Ameliorating Defects in Wide Bandgap Tin Perovskite Solar Cells Using Fluorinated Solvent and Hydrazide

Dhruba B. Khadka[1]*, Yasuhiro Shirai[1], Ryoji Sahara[2], Masatoshi Yanagida[1], and Kenjiro Miyano[1]

[1]Photovoltaic Materials Group, Center for GREEN Research on Energy and Environmental Materials, National Institute for Materials Science (NIMS), 1-1 Namiki, Tsukuba, Ibaraki 305-0044, Japan
[2]Computational Structural Materials Group, Research Center for Structural Materials, National Institute for Materials Science (NIMS), 1-2-1, Sengen, Tsukuba, Ibaraki 305-0047, Japan
Corresponding Author
*E-mail: KHADKA.B.Dhruba@nims.go.jp

ABSTRACT

Surface passivation with multifunctional molecules is an effective strategy to mitigate the defect and improve the performance and stability of perovskite solar cells (PSCs). Here, we report the fabrication of a wide band gap-PSC with tin perovskite (WB-Sn-HP; bandgap: 1.68 eV), followed by molecular surface passivation using 4-Fluoro-benzohydrazide (F-BHZ). WB-Sn-PSC has demonstrated a promising device efficiency of 11.14% with improved device stability. The key to enhancing device performance lies in the meticulous engineering of both surface and bulk properties of WB-Sn-HP film with F-BHZ treatment as a consequence of stronger electrostatic potential and molecular interaction with hydrazine and carbonyl functionalities. A compact perovskite film and highly crystalline film growth resulted in a longer carrier lifetime and surface defect mitigation with the control of Sn^{2+} oxidation as supported by theoretical calculations. This work underlines the promising potential of chemical engineering to improve the device performance of WB-Sn-PSC and stability using multifunctional passivating molecules.

Keywords: Wide bandgap tin perovskite; lead-free; tin oxidation; device stability; surface passivation, tandem device.

1. Introduction

Perovskite solar cells (PSC) have garnered attention for tandem applications, particularly in perovskite/perovskite or Si/perovskite structures.[1,2] The tandem solar cells typically combine narrow bandgap halide perovskites (E_g ~1- 1.3 eV) as bottom cells with wide bandgap halide perovskites (E_g >1.6 eV) as top cells.[1,3] Silicon/perovskite achieved efficiencies of over 33.7%[4,5] using wide bandgap- PSCs (WB-PSCs) while perovskite/perovskite structure obtained over 28.5%.[6] However, the toxicity of the lead in the halide perovskite (HP) is an acute concern for broader acceptance. Pb-free alternatives, such as Sn- and Bi-based HP materials are projected as suitable alternatives to resolve the toxicity issue.[7–11] Recent reports show Sn-PSCs achieving efficiencies of over 15%.[12,13] But they typically have bandgaps of 1.3-1.4 eV which do not fall within the optimal bandgap range for top cells. Therefore, WB-Sn-HPs (E_g >1.6 eV) are needed for Pb-free Si/perovskite tandem applications.

Despite the importance of Pb-free WB-PSCs, only a few reports have been documented on WB-Sn-PSCs.[14] Kanatzidis and co-workers have reported a set of Sn-PSCs by X-site engineering and demonstrated a PCE ~5.73% using $MASnIBr_2$ of E_g~ 1.75 eV adopting mesoporous n-i-p structure.[15] Mono A-site i.e. Cs, MA, or FA-based Sn-PSCs demonstrated comparatively lower performance than mixed A-site.[16,17] For example, Hayase and co-workers have reported a series of works on Sn-PSCs[18,19] and WB-Sn-PSCs by adopting mixed A and X-site methods coupled with additive engineering and surface treatments.[20,21] Particularly, they achieved a PCE of 8.66% by hole transport engineering using a self-assembly monolayer in WB-Sn-HP derivative [$EDA_{0.01}(GA_{0.06}(FA_{0.8}Cs_{0.2})_{0.94})_{0.98}SnI_2Br$, E_g~1.62 eV] adopting from the previous report.[22] An antioxidant additive such as aromatic carboxylic acid molecules in WB-Sn-HP ($FA_{0.75}MA_{0.25}SnI_2Br$) resulted in a PCE of 10.35% with improved device stability.[23] Khang and co-workers reported a certified record PCE of 11.70% of WB-Sn-PSCs using 4-phenylthiosemicarbazide as a functional additive.[24] Moreover, albeit molecular passivation methods also have been popularly used in Pb-PSCs for surface chemistry modulation and defect passivation,[25–27] there are lack of surface passivation reports on Sn-PSCs or Pb-free halide-based absorber layers.[14] Diau and co-workers have reported a phenylhydrazinium thiocyanate in which phenylhydrazinium cation acts as a reducing agent for surface passivation of regular bandgap Sn-HP ($FA_{0.8}GA_{0.2}SnI_3$).[28] Similarly, Cao et al. have documented bottom passivation using potassium thiocyanate in $FA_{0.75}MA_{0.25}SnI_2Br$ -based WB-Sn-HP demonstrating a decent PCE of 11.17% by regulating crystallization and interface modulation.[29] Despite the rich knowledge in Pb-PSCs, the PCE reports on the Sn-PSCs are still far behind. These reports underscore the effectiveness of multifunctional

molecules as an additive or surface passivation for the improvement in device performance and stability of Sn-PSCs. There are multiple interconnected factors such as facile oxidation of Sn^{2+}, poor surface chemistry, deep defect, and mismatch of interfacial band alignment with the carrier transport layer.[3,30] These predominant issues in Sn-PSCs are being focused on material chemistry and photocarrier dynamics aspects for solving it.[14,31]

Herein, we report the fabrication of Pb-free perovskite solar cells of inverted device configuration using WB-Sn-HP derivative (FA, MA, PEA)SnI_2Br) of E_g ~1.68 combined with surface passivation with multifunctional molecule. It demonstrated among the best PCE of 11.14% with a significant increase in open circuit voltage ~ 0.928 to 1.036 V with 4-Fluoro-benzohydrazide (F-BHZ) modified perovskite films. The F-BHZ treatment on WB-Sn-HP film demonstrates the growth of compact and highly crystalline film after post-annealing. The molecular passivation results in a longer carrier lifetime and surface defect mitigation with the control of Sn^{2+} oxidation as supported by theoretical calculations. A detailed analysis elucidates the underlying mechanism for the betterment of device efficiency and stability of WB-Sn-PSCs.

2. Results and Discussion

2.1. Molecular Passivation and WB-Tin Perovskite Film Growth

The WB-Sn-HP films were fabricated by surface treatment (ST) using multifunctional F-BHZ molecule as depicted in Figure 1a, b. The electrostatic surface potential of the F-BHZ molecule has a higher electron density in the vicinity of oxygen and fluorine. This molecule contains hydrazide and carbonyl functionalities with strong reducing properties for inhibiting Sn^{2+} oxidation to Sn^{4+}.[32–34] Additionally, the electron-rich fluorine in F-BHZ interacts with halides or halide vacancy as illustrated in Figure 1c. Theoretical calculations confirm that the F-BHZ molecule strongly binds to the Sn-perovskite surface, as depicted in Figure 1d. Under optimal interaction conditions, the bond lengths between F-BHZ and the Sn-perovskite surface were calculated to be 2.33Å for O-Sn, 4.15 Å for F-I, and 4.80 Å for F-Sn. The shorter O-Sn bond length suggests a strong interaction, whereas the longer F-I and F-Sn bond lengths indicate weaker interactions with other molecules. Details of molecular interactions are discussed in the theoretical calculation sections. Importantly, we found that the ethanol is prone to dissolving the perovskite layer while surface coating. Therefore, instead of ethanol, the electron-rich solvent, trifluoroethanol (TFE) having a similar boiling point (77-80 ^oC) was used for stabilizing the WB-Sn-HP film's surface.[28]

To understand the effect of F-BHZ treatment on film growth, the surface morphology (Figure 1e-g and Figure S1) was examined. The WB-HP film treated with F-BHZ demonstrates a well-covered surface with more compact and smoother grains. A slight increase in grain size observed in the ST film (Figure 1f,g) is attributed to additional post-annealing. However, at higher concentrations of F-BHZ (Figure 1g), the film develops unevenly distributed small crystallites, indicating deleterious film quality.

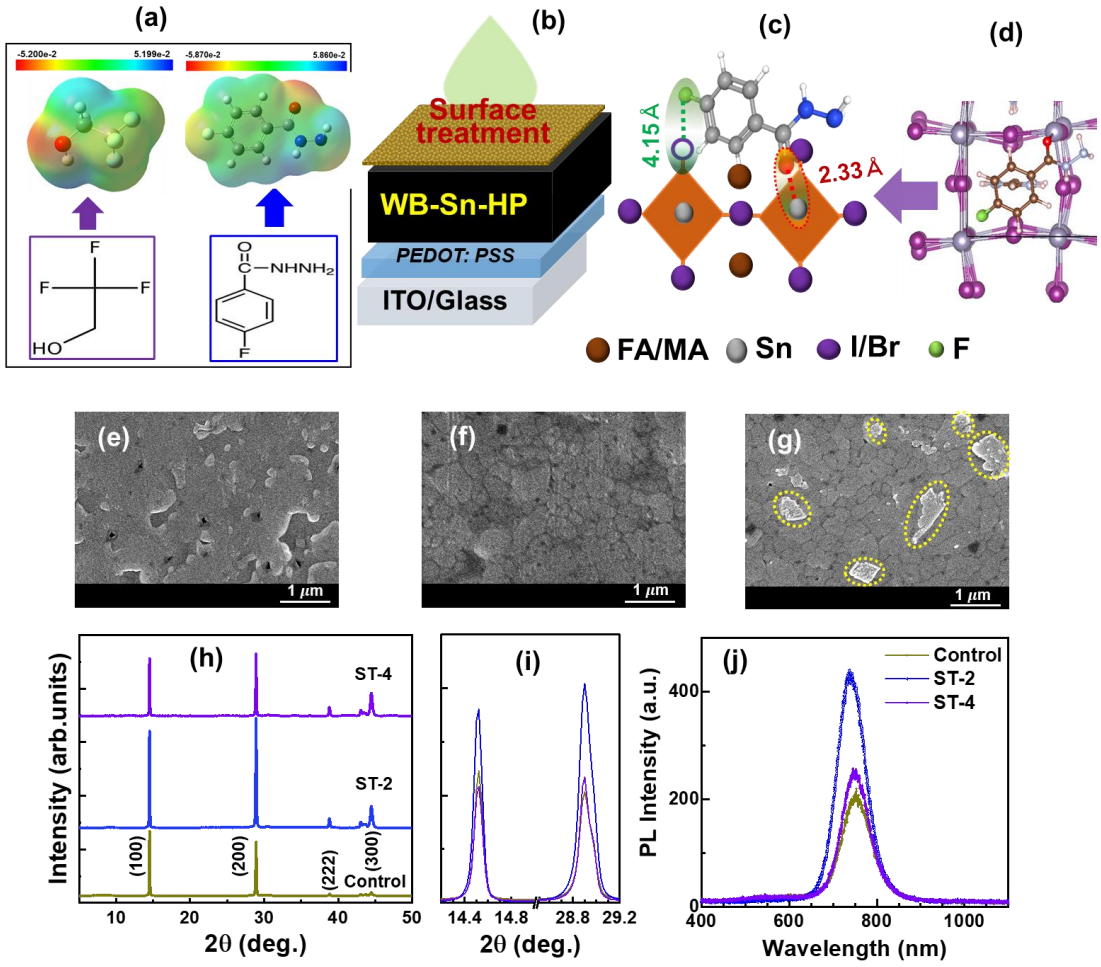

Figure 1. Schematic illustration of surface passivation; a) electrostatic surface potential of fluorinated solvent (trifluoroethanol) and hydrazide (4-Fluoro-benzohydrazide) (calculated from Gaussview6), b) surface treatment method, c) illustration of interfacial interaction of F-BHZ and tin perovskite surface, d) stabilized interaction of F-BHZ and perovskite surface adopted from DFT calculations. SEM images of WB-Sn-HP films with 4F-BHZ treatment with varying concentrations; (e) control (0 mg), (f) ST-2 (1 mg), and (g) ST-4 (2 mg/ml), yellow circles indicate uneven crystallites growth. h, i) XRD results, j) PL spectra of respective films.

The WB-Sn-HP films were characterized by X-ray diffraction (XRD) to understand whether the surface treatment affected the crystal structure of perovskite films. The XRD patterns (Figure 1h, i and Figure S2) show two prominent, highly oriented crystallographic planes: (100) and (200), which correspond to the orthorhombic phase. No shifting of characteristics XRD suggests no incorporation of surface treated molecule in the bulk crystal lattice (Figure S2c). Notably, the WB-Sn-HP film treated with F-BHZ treatment (ST-2) exhibited an intensified diffraction peak with a slightly narrower full width at half maximum (Figure S3) indicating betterment in crystallinity.

To investigate the impact on optophysical properties, we collected the photoluminescence (PL) spectra of WB-Sn-HP films deposited on the ITO substrate (Figure 1j, Figure S4a). The PL peaks are centered at 1.665 ±0.02 eV for the control and 1.672 ±0.02 eV for the ST film corresponding to their band gap edge (Figure S4), indicating slight blue shifting of bandgap with F-BHZ treatment. The PL intensity is significantly increased for the ST film, suggesting the mitigation of non-radiative carrier recombination in perovskite film.[35–37]

2.2. Device and Characteristics

To evaluate the surface treatment effect on the device, we fabricated WB-Sn-PSC with an inverted device configuration of ITO/PEDOT:PSS/WB-Sn-HP/ST(F-BHZ)/ICBA/BCP/Ag. The best current density–voltage (J–V) curves of WB-Sn-PSCs of control and optimal surface treatment are shown in Figure 2a. Table 1 compares the figures of merit. The control device demonstrated a power conversion efficiency (*PCE*) of 7.96%. The WB-Sn-PSC with F-BHZ (≤ 1 mg/ml) treated enhanced *PCE* to ~11.14% with a significant increase in open circuit voltage (V_{OC}) ~ 0.914 to 1.024 V and fill factor (*FF*) ~ 69.2 to 75.7%. Our champion result is among the best reports on WB-Sn-PSCs as listed in Table S2. The effect of the concentration of F-BHZ on device performance is shown in Figure. 1e. A statistical scenario of device parameters is given in supporting information (Figure 2b, Figure S5, and Table S1). Besides, WB-Sn-PSC treated with a higher concentration of F-BHZ (>1.5 mg/ml) lowers the efficiency. This decline is ascribed to the deterioration of film quality stemming from uneven film morphology induced during post-annealing with more concentrated passivated molecules. The remarkable improvement in device parameters is driven by compact film morphology, high crystalline quality, modulated surface chemistry, interface energy, and defect passivation. These properties will be discussed later in detail.

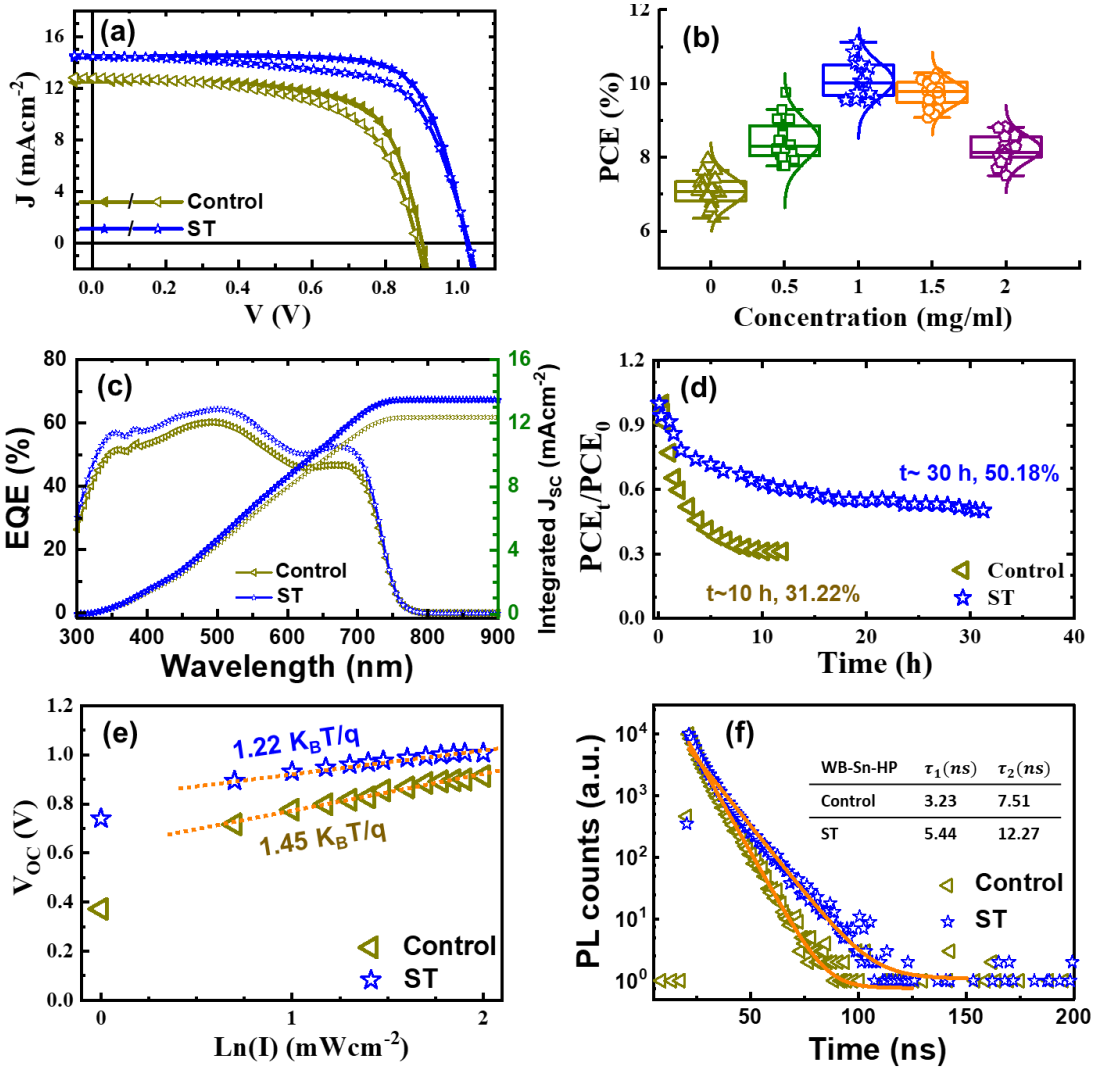

Figure 2. Device characteristics. a) *J–V* curves of the control and F-BHZ treated (optimal concentration; *x* = 1 mg/ml) WB-Sn-PSCs; (filled/unfilled symbols stand for forward/reverse scan direction). b) Statistics of *PCE* of the devices with surface treatment. These data consist of 20 devices for each condition from five batches. c) *EQE* spectra. d) Operational stability of WB-PSCs. e) Light intensity dependence of V_{OC}. f) TRPL decay spectra.

Table 1. Summarized device parameters of the WB-Sn-PSCs (control and ST) under one sun illumination. The best device parameters and the average values of *PCE* and standard deviation (SD) (20 devices from 4 batches).

Device	Scan direction	J_{SC} ($mAcm^{-2}$)	V_{OC} (V)	*FF*	*PCE* (%)	*PCE* Average ± SD
Control	F	12.58	0.914	0.692	7.96	7.09 ± 0.41
	R	12.76	0.928	0.622	7.37	
ST	F	14.37	1.024	0.757	11.14	10.58 ± 0.39
	R	14.46	1.036	0.696	10.43	

Figure 2c depicts the external quantum efficiency (*EQE*) spectra, where the short circuit current density (J_{SC}) values (12.36 and 13.48 mA/cm^2 for the control and ST devices) from integrated EQE curves are in the range of the value obtained from the *J–V* curves. It demonstrates a higher EQE spectrum over wider wavelength regimes. Both the control and F-BHZ-treated perovskite films exhibit minimal changes in their absorption spectra (Figure S6), with only slight variations observed at the band edge and within the green wavelength region. This suggests that the improvements in the EQE spectra are not primarily due to differences in absorption. Instead, the increased EQE can be attributed to enhanced interface and bulk quality resulting from surface passivation with F-BHZ multifunctional molecules, corroborating the quantitative analysis of EQE spectra reported by Fujiwara and co-workers. [38] The band edges extracted from *EQE* spectra (Figure S7) show a value of 1.682 and 1.683 ±0.02 eV for the control and ST device. This aligns with the bandgap estimation from the characteristic PL peak and absorption spectra.

To assess the device stability, we monitored the operational stability of the control and ST devices under maximum power point tracking (MPPT) conditions and air ambient. The device with F-BHZ showed comparatively better operational device stability (Figure 2d). The control device's PCE lowered to <31.22% of the original PCE after 10 hours while the ST device held its PCE to ~50.18% of the initial PCE after 30 hours. These device results suggest that the surface treatment with F-BHZ is propitious for the enhancement of device performance as well as the device's stability. The improvement in device stability is attributed to the passivation of the surface and grain boundary defects with F-BHZ treatment resulting in the non-radiative recombination and oxidation of Sn^{2+} to Sn^{4+}. The details of this phenomenon will be discussed in succeeding sections. Indeed, addressing the constraints on device parameters and operational stability remains a significant challenge, necessitating substantial further effort.

To gain insights into the charge recombination behaviors in the WB-Sn-PSC,[37] the light-intensity-dependent V_{OC} was analyzed. As depicted in Figure 2e, a higher slope of the control device (1.45 k_BT/q) compared to the ST device (1.22 k_BT/q) corroborates a reduction in trap-assisted recombination in the WB-Sn-PSC with F-BHZ treatment.[39] To shed light on carrier recombination, we collected time-resolved photoluminescence (TRPL) responses (Figure. 2f).[40] WB-Sn-HP film with F-BHZ shows a longer carrier lifetime (τ_1 ~ 5.44; τ_2 ~12.27 ns) compared to the control film (τ_1 ~ 3.23; τ_2 ~7.51 ns). Short (τ_1) and longer (τ_2) lifetime account for the interface and bulk quality.[41] A higher lifetime value corroborates the fact that the recombination pathways in the control film have been suppressed to some extent by surface treatment with F-BHZ. It is attributed to the mitigation of recombination densities on the WB-Sn-HP film by modulating the surface defect chemistry with the F-BHZ passivation molecule.

2.3. Effect on Molecular Passivation on Surface Properties

To investigate the interfacial energy modulation, we characterized the film using ultraviolet photoelectron spectroscopy (UPS). The onset energy i.e. between the valence band and Fermi level ($\Delta E_{F,V} = E_V - E_F$) (Figure 3a,b) was found to be shallower for the ST film (0.746 eV) compared to the control film (1.307 eV). It shows an increase in work function (ϕ) for WB-Sn-HP film with ST (Figure 3b,d). These results suggest that surface energy modulation induces more p-type characteristics with the F-BHZ treatment. The band structure (Figure S8a) constructed by accounting for the bandgap extracted from EQE shows a downshifting of HOMO and LUMO levels for the WB-Sn-HP film with ST. The energy band of the device (Figure S8b) reveals the LUMO level offsets to ICBA changed from -0.05 and -0.22 eV, while HOMO level offsets to the PEDOT:PSS are +0.48 and +0.64 eV. These results suggest a thin energy spike on the surface which induces a band offset only at the Sn-HP/ICBA interface. It is reported that a thin spike at the interfacial band is beneficial for mitigating interfacial recombination.[42] Additionally, the WB-Sn-PSCs with PCBM showed an improved PCE for Sn-PSC upon F-BHZ treatment, increasing from ~ 6.39 % in the control to 9.15 % for ST (see supporting information, Figure S9a,b, and Table S3). The enhanced device performance for the ICBA device is attributed to favorable band alignment (Figure S9c), which partially contributes to the improvement in device parameters of WB-Sn-PSCs with F-BHZ treatment. These results underscore that surface energy modulation of WB-Sn-HP film with F-BHZ treatment can enhance device parameters, thereby partially supporting the observed improvement in device performance.

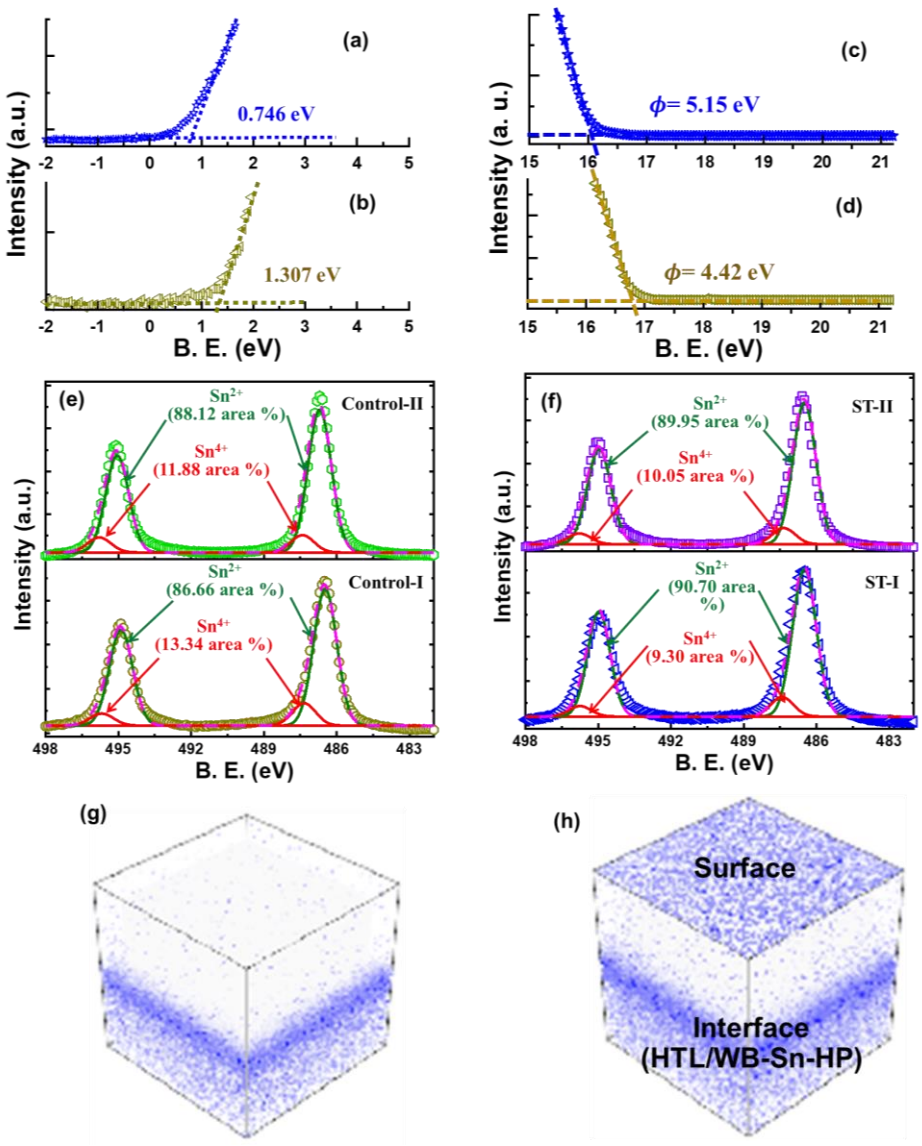

Figure 3. UPS spectra of the control and ST WB- Sn-HP films; a, b) valence band spectra with the energy difference between the valence band maximum (E_V) and the Fermi level (E_F). c, d) photoemission cutoff energy. XPS-spectra of Sn 3d: $3d_{5/2}$ and $3d_{3/2}$ (surface-I and depth-II) for e) control and f) ST WB-Sn-HP film surface. F-BHZ $(O = C - N)^-$ distribution 3D image reconstructed from the ToF-SIMS depth profiles; g) control and h) ST film.

To study the effect on surface chemistry, we analyzed the films by X-ray photoelectron spectroscopy (XPS) (Figure S10). We analyzed the deconvolution of the Sn XPS peaks into the Sn 3d (3d5/2 (3d3/2)) (Figure 3e,f) at ~486.7 (495.2) for the Sn^{2+} and 487.3 (495.7) eV for Sn^{4+}. On the film surface, the ionic percentage of Sn^{4+} in the WB-Sn-HP with F-BHZ is suppressed from 13.34 to 9.30%. Those values are found to be 11.88% and 10.05 % for the control and surface-treated film in the depth to ≥10 nm. These results corroborate that surface

treatment of WB-Sn-HP with F-BHZ effectively controls the extent of facile oxidation. Besides, the characteristic XPS spectra for Sn^{2+} shift toward higher binding energy for the ST with F-BHZ which is attributed to the stronger interaction between SnI_2 and F-BHZ (Sn^{2+}–$NHNH_2$ and Sn^{2+}–O═C bonding). F-BHZ can form a strong coordination complex with Sn^{2+} and SnI_2 frame controlling the extent of oxidation on the surface and bulk of the Sn-HP film. Hence, it mitigates notorious defect chemistries on the film's surface resulting in better film quality and hence device performance.[43]

Furthermore, time-of-flight secondary ion mass spectrometry (ToF-SIMS) was carried out to profile the distribution of key elements in the control and target film (Figure S11). A set of 3D image profiles of the negative ion $(O = C - N)^-$ ion from F-BHZ (Figure 3g,h) displays the distribution of F-BHZ molecules. For the control film, the distribution at the PEDOT:PSS/WB-Sn-HP interface is assigned to the corresponding negative ions from the PEDOT:PSS. The F-BHZ molecule uniformly covers up the surface of the WB-Sn-HP film with a slight diffusion to the bulk through the grain boundary. This observation aligns with other reports.[40,44] This supports the suppression of Sn oxidation and defect chemistries in surface-treated WB-Sn-HP film.

2.4. Transient Photo-characteristics and Capacitance Analysis

Furthermore, transient device characteristic measurements were performed to investigate photocarrier dynamics. The transient photovoltage (TPV) of the respective device is given in Figure 4a. The TPV decay curves demonstrate that the ST device (22.42 μs) has a longer carrier lifetime compared to the control device (~13.65 μs), indicating a reduction in trap-assisted recombination. These characteristic results agree with the device results with the F-BHZ. These observations are parallel to other reports.[33,45] To evaluate the interface quality, we also measured the transient photocurrent (TPC) of devices by modulating the transient illumination (I) and voltage bias (II). In TPC curves (Figure 4b), the I- regime (Figure S12a) shows a shorter lifetime for the ST device (2.34 μs) compared to the control device (2.88 μs) suggesting a faster carrier extraction due to better interface quality in the ST device. On the other hand, the II-regime carrier extraction under voltage bias (Figure S12b) demonstrates a prolonged lifetime (2.80 μs) for the ST which is attributed to fewer recombination traps at the interface or bulk. These characteristic results support materials and device characteristics.

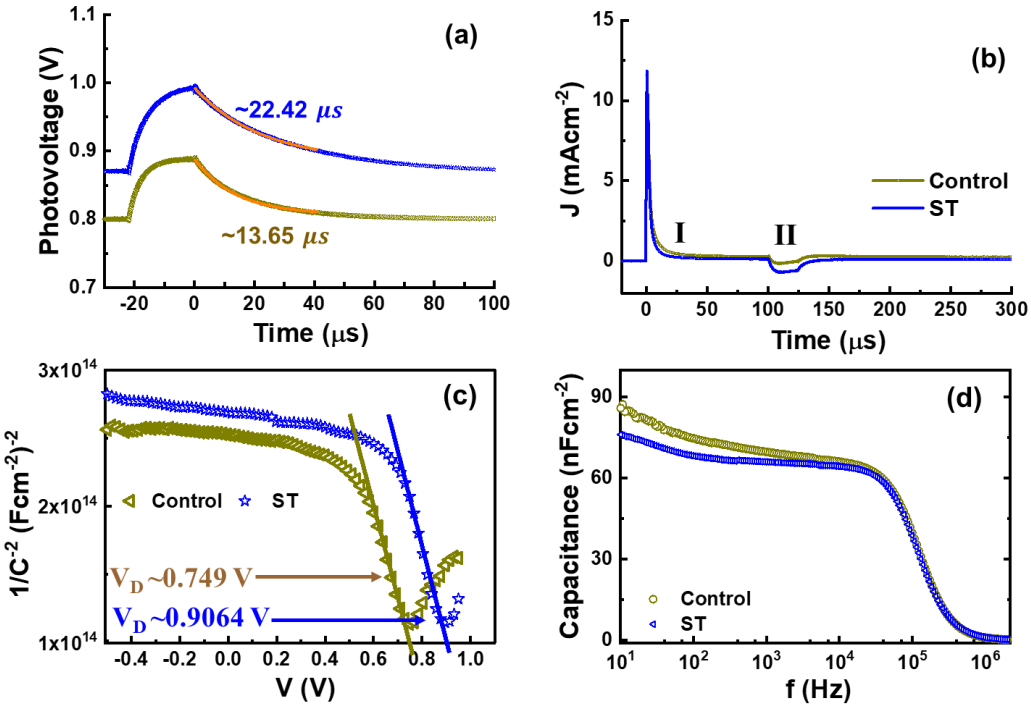

Figure 4. Analysis of device characteristics: Transient characteristics; a) TPV decay curves. b) TPC decay curves. Admittance analysis; c) M–S plots, d) *C–f* spectra under dark.

To gain a more comprehensive understanding of the defect profile and junction potential, we analyze the capacitance characteristics of the WB-Sn-PSCs. This assesses the surface treatment effect on carrier distribution, comprising free carrier and defect density.[46] It also accounts for the accumulation of ions and charges at the interface in thin-film solar cells.[47] Figure 4c shows the Mott-Schottky (*M-S)* plots WB-Sn-PSCs. A fully depleted M-S curve implicates a well-defined p-i-n junction quality. It reveals an increase in diffusion potential (V_D)[37] from 0.749 V (for the control) to 0.906 V for the surface treatment device, consistent with the higher V_{OC} observed in the F-BHZ-treated device. The C-V profile (Figure S13a) shows the bulk carrier density (N_{CV}^{B}) decreased from ~15.36×10^{15} cm^{-3} in the control device to ~10.28×10^{15} cm^{-3} in the device with surface treatment. Likewise, the C-V carrier profile at the edge, which incorporates the interfacial defect profile (N_{CV}^{IF}) is found to be reduced by approximately half in the device with F-BHZ surface passivation (10.98×10^{17} to 5.42×$10^{17}$$cm^{-3}$). The *C-V* profile result corroborates that the surface treatment with F-BHZ passivates the defect densities in the bulk at the space charge region and interface.

Furthermore, the capacitance-frequency (*C-f*) spectra also signify the defect status in a device.[40,47] Figure 4d exhibits a slightly greater capacitance in the 1-50 kHz range,

characterized by a plateau region attributed to the WB-Sn-HP bulk layer, implying a higher defect density in the control device. The capacitance continues to increase in further lower frequency regimes which is related to ionic motion or charge accumulation. It corroborates that the surface treatment reduces the ionic or charge accumulation in the WB-Sn-PSC. The results from capacitance analysis align with the observation of a prolonged carrier lifetime indicated by TRPL and TPV curves, as well as with the decrease in the extent of Sn^{2+} oxidation observed in the XPS analysis. Besides, we also evaluated the C–f spectra under light (Figure S13b). It exhibits a notably higher capacitance at low frequencies compared to high frequencies regime indicating a prevalence of photogenerated carriers or ions. A comparatively lower capacitance for the surface-treated WB-Sn-PSC corroborates a suppression of ionic motion at the interface or electrode. This implicates a robust interfacial junction that supports the improved stability of WB-Sn-PSC with F-BHZ treatments. Thus, our work underscores that the surface treatment with stronger electrostatic and dipole-rich passivating molecules has a vital role in the improvement of the device's performance and stability.

2.5. Theoretical Calculations: Molecular Interaction and Defect

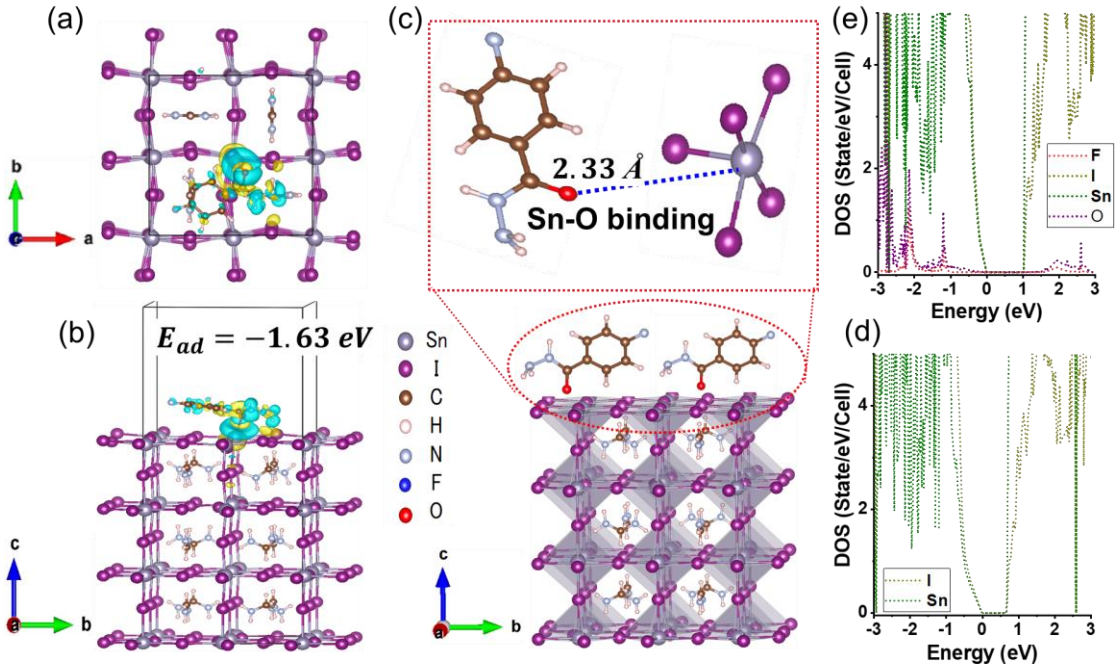

Figure 5. Top view (a) and side view of the optimized structure of Model 1 (b), with the molecule laying on the back on the substrate as the initial position with the most stable energy among the present models[48]. The E_{ad} and the optimal orientation for surface molecular

interaction with O-Sn (bond length is 2.33Å) (c). The atom-projected density of states without (d) and with (Model 1) the molecule (e). Where the Fermi energy is set at energy zero.

Moreover, to get into the theoretical insights on the effect of the F-BHZ molecule on the Sn-HP surface, First-principles calculations based on density functional theory (DFT) were performed adopting a slab model of a SnI_2-terminated surface (Figure S14)[33]. The details of the calculations are described in the Supporting Information. Figure 5a demonstrates the optimized structure with surface passivating molecule. The molecule is found to be most stable when the O of the F-BHZ molecule interacts with the Sn site with an O-Sn bond length is 2.33 Å and the corresponding adsorption energy (E_{ad}) = − 1.63eV/system (Figure 5b,c). The surface interaction was confirmed with different defined settings varying E_{ad} for F-Sn interaction (-0.62 eV; Figure S15) and O-Sn interaction (-1.27 eV; Figure S16, -1.47 eV; Figure S17) The DOS for the case of without and with the F-BHZ molecule (Figure 5d,e) indicates that the presence of F-BHZ does not introduce any in-gap states that could negatively impact the device's performance. Theoretical calculations confirm that the F-BHZ molecule forms a strong interaction with the Sn-HP surface, particularly through the oxygen atom. We found that the F-BHZ molecular interaction modulates the mid-gap DOS of the control film (Figure 5e and Figure S18). It corroborates the defect quenching as observed in capacitance and TRPL analysis.

Thus, theoretical and experimental analyses indicate that F-BHZ molecules adsorb strongly onto the Sn-perovskite surface, effectively suppressing Sn^{2+} oxidation and ion migration during illumination. These findings align with experimental data showing improvements in both device performance and stability, thereby providing a solid theoretical basis for the observed enhancements.

3. Conclusion

This work has demonstrated a post-surface treatment method on wide band gap tin perovskite film (1.68 eV) for improving the device's performance and stability. We achieved an improvement in device efficiency from ~ 7.96 % for the control to 11.14% for the F-BHZ-treated WB-Sn-PSC with a significant increase in device parameters (V_{OC} ~ 0.914 to 1.024 V, *FF* ~ 69.2 to 75.7% and J_{SC} 12.58 to 14.37 $mAcm^{-2}$) and improvement in device stability. It is found that the F-BHZ treatment ameliorates the surface chemistry of perovskite film and interface energy via chemical interaction with functional molecular bonding. The surface passivated film controls the Sn^{2+} oxidation and mitigates the defect with uniform distribution

of the F-BHZ molecule on WB-Sn-HP film as confirmed by ToF-SIMS analysis. A detailed analysis of the lifetime extracted from transient characteristics substantiates the passivation of trap-assisted recombination and betterment in interface quality, as supported by capacitance analysis and DFT calculations. Thus, this work paves the way for developing efficient and stable WB-Sn-PSC by modulating the defect chemistry with chemical engineering.

4. Experimental Section

Materials used: All chemicals were purchased from commercial suppliers as mentioned and unless otherwise specified, they were used as received. Formamidinium bromide (FABr, TCI), Methylammonium bromide (MABr, ≥99%, Sigma Aldrich), 4-Fluoro-benzo hydrazide (4F-BHZ, >98%, TCI), SnI_2 (99.999%, Sigma Aldrich), and SnF_2 (99 %, Sigma Aldrich), Sn-powder (nanopowder, <150 nm particle size, ≥99%, Sigma Aldrich) Phenethylammonium bromide (PEABr; >98%, TCI), Trifluoroethanol (TFE, >99%, TCI), poly(3,4-ethylenedioxythiophene):poly(styrene sulfonate) (PEDOT: PSS PEDOT:PSS (Clevious, A14083), indene-C60 bisadduct (ICBA) (TCI, 99% purity), [**6**,**6**]-Phenyl-**C** 61-Butyric Acid Methyl Ester (PCBM) (TCI, 99% purity), and Bathocuproine (BCP) (Sigma Aldrich, 99% purity) were purchased and used as received.

Device Fabrication: Pre-cleaned ITO glass substrates were treated with UV-ozone for 15 min. Then PEDOT: PSS with 50% diluted by methanol was spin-coated on at 4000 rpm for 30 s and annealed at 150 °C for 20 min in the air. Afterward, the PEDOT: PSS substrates were transferred into a N_2-filled glovebox. WB-Sn-based HP deposition, the precursor solution (0.85 M) was prepared by dissolving FABr (0.75), MABr (0.1), PEABr (0.15), SnI_2 (1), SnF_2 (0.1), Sn-powder (5 mg) in mixture of solvents (dimethylformamide (DMF) and dimethyl sulfoxide (DMSO) in 4:1 ratio). The precursor solution was spin-coated at 6000 rpm for 90 s and chlorobenzene (CB) of 0.70 ml was dripped as the anti-solvent at 60^{th} seconds during the spinning process. Then, the films were annealed at 70 °C for 5 min for crystallization. For surface treatment, the precursor solution was prepared by dissolving 4-Fluoro-benzo hydrazide (F-BHZ) of concentrations: 0.5, 1, 1.5, and 2 mg/ml by dissolving in trifluoroethanol (TFE). The precursor was spin-coated at 5000 rpm for 50 s (2 s slope) at the beginning and end. These surface-treated films were baked at 70 °C for 5 min. For ETL deposition, ICBA (18 mg/mL, dissolved in CB) was spin-coated at 1000 rpm-30 s, 5000 rpm-5 s, and annealed at 75 °C for 5 min. BCP (1 mg/ml in isopropanol) is deposited by spin coating at 5000 rpm -20 s (2 s -slope) and annealed at 70 °C for 5 min. Finally, Ag (150 nm) was thermally deposited as a metal electrode. Devices with an area of ~0.26 cm^2 were sealed using UV-curable resins before the subsequent measurements in ambient conditions.

Device Characterizations: In NIMS Battery Research Platform facilities, X-ray diffraction (XRD) patterns of fabricated Sn-HaP films were collected using an advanced X-ray diffractometer (Rigaku SmartLab, CuK_α radiation, λ = 1.54050 A). X-ray photoelectron spectroscopy (XPS) spectra were

obtained using a Versa Probe II (ULVAC-PHI, Japan). Perovskite film samples for XPS measurements were prepared in an N_2-filled glove box and transferred to the XPS chamber through an N_2-filled transfer vessel to avoid oxygen contamination. XPS with a nonmonochromatic source was measured (Al Kα; 1486.6 eV, spot size 10-300 μm) at a pass energy of 187.85 eV (1.5 eV step size) for the survey scan and pass energy 46.95 eV (0.1 eV step size) for the fine scan with spot size 100 μm. The XPS spectra were calibrated with the binding energy of 284.8 eV for C1s.

In NIMS Namiki foundry research facilities, the morphology of films and cross-sectional images were taken by a high-resolution scanning electron microscope (SEM) at 5 kV accelerating voltage (Hitachi, S-4800). The photoluminescence (PL) spectra were collected using a micro-PL spectrometer (HORIBA, LabRamHR-PL NF(UV-NIR)) ~532 nm laser diode (10 $mWcm^{-2}$) as an excitation source. The carrier lifetimes were measured with a fluorescence lifetime spectrometer (Quantaurus-τ from Hamamatsu-Photonics K.K., C11367) equipped with ~405 nm laser diode (typical peak power of 400 mW) at 200 kHz repetition rate. The absorption spectra films were measured using a UV-Vis-NIR spectrometer (UV-2600i, Shimadzu). The absorption spectra and photoluminescence (PL) spectra of various films were measured using a UV-Vis-NIR spectrometer (UV-2600i, Shimadzu). The band structure of the film was measured using Ultraviolet photoelectron spectroscopy (UPS, Thermo Fisher Scientific, Inc.) with a He I line (21.22 eV) from a helium discharge lamp.

The current density–voltage (J–V) curves were measured at the scan rate of 0.05V/s under 1 sun with an AM1.5G spectral filter (100 mW/cm^2) coupled with an MPPT system (Systemhouse Sunrise Corp.). The light intensity was calibrated by a silicon (Si) diode (BS-520BK). For the stability test, the encapsulated devices were measured at MPPT conditions. The J–V curves were measured with a scan rate of 0.05 V/s under 1 sun with an AM 1.5G spectral filter (100 mW cm^{-2}) coupled with an MPPT system (Bunkoukeiki Corp. The devices were kept under 1-Sun intensity under MPPT conditions (35–40% RH, ~room temperature) during device stability monitoring. BIR-50 solar cell light resistance test system, incubator type 50×50 mm irradiation, Systemhouse Sunrise Corp.). The external quantum efficiency (EQE) spectra were obtained using a spectrometer (SM-250IQE, Bunkokeiki, Japan).

Time-of-flight secondary ion mass spectrometry (ToF-SIMS) measurements were carried out using a ToF.SIMS 5 (ION-TOF GmbH) instrument equipped with a 60 keV and pA current Bi^{2+} beam for analysis and a 10 keV and nA current Ar gas cluster ion beam (Ar-GCIB) for sputtering in non-interlaced mode to have minimal interfacial mixing. The sputtered area was 700 × 700 μm^2 and the analysis area was 100 × 100 μm^2.

A commercial PAIOS system (PAIOS V.4.3) was used for the transient photovoltage and photocurrent decay measurement. A pulse intensity was used to induce a spike in photovoltage. The capacitance spectra (C-f) were taken from PAIOS v. 4.3 software, which scans from 20 Hz to 2 MHz at 30 mV AC in the dark at a bias voltage of 0 V. capacitance–voltage (C–V) measurements were carried out at 20 kHz under dark condition (the geometric capacitance regime in C–f spectra).

Density functional theory calculation: First-principles calculations based on density functional theory (DFT) were performed by adopting a slab model of a SnI_2-terminated surface[33] using the Vienna ab initio simulation package[49] which implements the projector-augmented wave method[50]. The influence of vdW interactions between the F-BHZ molecules and Sn-HP film was considered.

For the exchange-correlation function, the Perdew–Burke–Ernzerhof function[33], was used. A $\sqrt{2} \times \sqrt{2} \times 2$ slab supercells of (001) surface, containing 7 layers were built from a bulk tetragonal phase of $FASnI_3$ (space group: P4/mbm). with a vacuum region of about 13- 19 Å was added in the z direction depending on the orientation of the molecule. The kinetic energy cutoff of 500 eV and the convergence criterion of 10^{-5} eV for the self-consistent loop were employed. To explore stable adsorption sites of the molecule, a SnI_2-terminated surface was used, on which a molecule was placed at various initial in-plane (xy-plane) positions with different molecular orientations as follows: In the present study, four different molecular orientations were considered concerned with the surface, based on the insight in the previous work[51]: Model 1 where the molecule laying on the back, Model 2 where the molecule laying on the back, Model 3 where the molecule laying on its side, and Model 4 with a standing molecule. We first placed one molecule on the surface at the blue-colored × sites in Figure S14(a). Furthermore, considering the test calculations, additional simulations were performed for Model 1, which generally shows relatively stable energy compared with other Models, at the red colored × sites (see Figure S14(a)) for a more detailed analysis. Because of the symmetry of the structure, the number of the combination of the orientation of the molecule and the surface could be reduced. From these initial configurations, we optimized the whole system except for the lowest two layers of the substrate. For the Brillouin zone integration, Gamma point sampling for the isolated molecule, the $2 \times 2 \times 1$ k point sampling for the system with and without molecule on the substrate were employed for the structural relaxation, and the $4 \times 4 \times 2$ k point mesh was used for the subsequent DOS calculations. The adsorption energy of the molecule was evaluated as $E_{ads} = E_{\text{system with molecule}} - E_{\text{system without molecule}} - \mu_{mol}$ where $E_{\text{system with molecule}}$ and $E_{\text{system without molecule}}$ are energies of the surfaces with and without a molecule additive, respectively, and μ_{mol} is the chemical potential of the molecule. The total energy computed for an isolated gas phase was used for μ_{mol}.

Figures S15-17 show the optimized structure of Model 2, Model 3, and Model 4 with their adsorption energies and bond length between O-Sn (for Model 2 and Model 3) and F-Sn (for Model 4), respectively.

Supporting Information

Supporting Information is available from the Wiley Online Library or the author.

AUTHOR INFORMATION

Corresponding author.

*Email:KHADKA.B.Dhruba@nims.go.jp (D.B.K.)

ORCID

Dhruba B. Khadka: 0000-0001-9134-3890
Yasuhiro Shirai: 0000-0003-2164-5468
Masatoshi Yanagida: 0000-0002-8065-7875
Ryoji Sahara: 0000-0003-0788-2985
Kenjiro Miyano: 0000-0002-5869-3087

Notes

The authors declare no competing financial interest.

Acknowledgments

This work was supported by The Hitachi Global Foundation, Kurata grant #1572. R.S. was supported by the Japan Society for the Promotion of Science (JSPS) KAKENHI (Grant No. 24K01149). The calculations in this study were performed using the Numerical Materials Simulator at the National Institute for Materials Science (NIMS); the MASAMUNE supercomputing system at the Center for Computational Materials Science, Institute for Materials Research (IMR), Tohoku University (Proposal No. 2202312-SCKXX-0502).
The authors are grateful to Yamaguchi Kazuo-San (XPS), Dr. Hitoshi Ota (XRD), and Nariaki Sato-San (ToF-SIMS) from the NIMS battery research platform for the technical support for respective measurement and analysis.

References

[1] F. Fu, J. Li, T. C. Yang, H. Liang, A. Faes, Q. Jeangros, C. Ballif, Y. Hou, *Adv Mater* **2022**, *34*, 2106540.

[2] P. Wu, D. Thrithamarassery Gangadharan, M. I. Saidaminov, H. Tan, *ACS Cent Sci* **2023**, *9*, 14.

[3] D. B. Khadka, Y. Shirai, M. Yanagida, J. W. Ryan, Z. Song, B. G. Barker, T. P. Dhakal, K. Miyano, *Solar RRL* **2023**, *7*, 2300535.

[4] E. Aydin, E. Ugur, B. K. Yildirim, T. G. Allen, P. Dally, A. Razzaq, F. Cao, L. Xu, B. Vishal, A. Yazmaciyan, A. A. Said, S. Zhumagali, R. Azmi, M. Babics, A. Fell, C. Xiao, S. De Wolf, *Nature* **2023**, *623*, 732.

[5] G. Szabó, N.-G. Park, F. De Angelis, P. V. Kamat, *ACS Energy Lett* **2023**, *8*, 3829.

[6] R. Lin, Y. Wang, Q. Lu, B. Tang, J. Li, H. Gao, Y. Gao, H. Li, C. Ding, J. Wen, P. Wu, C. Liu, S. Zhao, K. Xiao, Z. Liu, C. Ma, Y. Deng, L. Li, F. Fan, H. Tan, *Nature* **2023**, *620*, 994.

[7] W. Ke, C. C. Stoumpos, M. G. Kanatzidis, *Adv Mater* **2019**, *31*, 1803230.

[8] D. B. Khadka, Y. Shirai, M. Yanagida, K. Miyano, *J Mater Chem C Mater* **2020**, *8*, 2307.

[9] D. B. Khadka, Y. Shirai, M. Yanagida, K. Miyano, *J Mater Chem C Mater* **2019**, *7*, 8335.

[10] M. G. M. Pandian, D. B. Khadka, Y. Shirai, S. Umedov, M. Yanagida, S. Subashchandran, A. Grigorieva, K. Miyano, *J Mater Chem C Mater* **2020**, *8*, 12173.

[11] K. Nishimura, M. A. Kamarudin, D. Hirotani, K. Hamada, Q. Shen, S. Iikubo, T. Minemoto, K. Yoshino, S. Hayase, *Nano Energy* **2020**, *74*, 104858.

[12] J. Chen, J. Luo, E. Hou, P. Song, Y. Li, C. Sun, W. Feng, S. Cheng, H. Zhang, L. Xie, C. Tian, Z. Wei, *Nat Photonics* **2024**, *18*, 464.

[13] Y. Shi, Z. Zhu, D. Miao, Y. Ding, Q. Mi, *ACS Energy Lett* **2024**, *9*, 1895.

[14] W. J. Jang, H. W. Jang, S. Y. Kim, *Small Methods* **2024**, *8*, 2300207.

[15] F. Hao, C. C. Stoumpos, D. H. Cao, R. P. H. Chang, M. G. Kanatzidis, *Nat Photonics* **2014**, *8*, 489.

[16] T. Bin Song, T. Yokoyama, C. C. Stoumpos, J. Logsdon, D. H. Cao, M. R. Wasielewski, S. Aramaki, M. G. Kanatzidis, *J Am Chem Soc* **2017**, *139*, 836.

[17] T. Yokoyama, T.-B. Song, D. H. Cao, C. C. Stoumpos, S. Aramaki, M. G. Kanatzidis, *ACS Energy Lett* **2017**, *2*, 22.

[18] M. A. Kamarudin, D. Hirotani, Z. Wang, K. Hamada, K. Nishimura, Q. Shen, T. Toyoda, S. Iikubo, T. Minemoto, K. Yoshino, S. Hayase, *J Phys Chem Lett* **2019**, *10*, 5277.

[19] L. Wang, Q. Miao, D. Wang, M. Chen, H. Bi, J. Liu, A. K. Baranwal, G. Kapil, Y. Sanehira, T. Kitamura, T. Ma, Z. Zhang, Q. Shen, S. Hayase, *Angewandte Chemie* **2023**, *135*, e202307228.

[20] M. Chen, M. A. Kamarudin, A. K. Baranwal, G. Kapil, T. S. Ripolles, K. Nishimura, D. Hirotani, S. R. Sahamir, Z. Zhang, C. Ding, Y. Sanehira, J. Bisquert, Q. Shen, S. Hayase, *ACS Appl Energy Mater* **2021**, *4*, 5615.

[21] M. Chen, G. Kapil, Y. Li, M. A. Kamarudin, A. K. Baranwal, K. Nishimura, S. R. Sahamir, Y. Sanehira, H. Li, C. Ding, Z. Zhang, Q. Shen, S. Hayase, *J Power Sources* **2022**, *520*, 230848.

[22] M. Chen, G. Kapil, L. Wang, S. Razey Sahamir, A. K. Baranwal, K. Nishimura, Y. Sanehira, Z. Zhang, M. Akmal Kamarudin, Q. Shen, S. Hayase, *Chemical Engineering Journal* **2022**, *436*, 135196.

[23] F. Hu, C.-H. Chen, Y.-H. Lou, T.-Y. Teng, Y.-R. Shi, Y. Xia, K.-L. Wang, J. Chen, Z.-K. Wang, L.-S. Liao, *J Mater Chem A Mater* **2023**, *11*, 4579.

[24] P. Pandey, S. Cho, J. Bahadur, S. Yoon, C. Oh, I. Hwang, H. Song, H. Choi, S. Hayase, J. S. Cho, D. Kang, *Adv Energy Mater* **2024**, *14*, 2401188.

[25] L. Yang, J. Feng, Z. Liu, Y. Duan, S. Zhan, S. Yang, K. He, Y. Li, Y. Zhou, N. Yuan, J. Ding, S. (Frank) Liu, *Adv Mater* **2022**, *34*, 2201681.

[26] S. Gharibzadeh, P. Fassl, I. M. Hossain, P. Rohrbeck, M. Frericks, M. Schmidt, T. Duong, M. R. Khan, T. Abzieher, B. A. Nejand, F. Schackmar, O. Almora, T. Feeney, R. Singh, D. Fuchs, U. Lemmer, J. P. Hofmann, S. A. L. Weber, U. W. Paetzold, *Energy Environ Sci* **2021**, *14*, 5875.

[27] D. B. Khadka, Y. Shirai, M. Yanagida, T. Tadano, K. Miyano, *Adv Energy Mater* **2022**, *12*, 2202029.

[28] E. Jokar, H.-S. Chuang, C.-H. Kuan, H.-P. Wu, C.-H. Hou, J.-J. Shyue, E. Wei-Guang Diau, *J Phys Chem Lett* **2021**, *12*, 10106.

[29] J.-J. Cao, Y.-H. Lou, W.-F. Yang, K.-L. Wang, Z.-H. Su, J. Chen, C.-H. Chen, C. Dong, X.-Y. Gao, Z.-K. Wang, *Chemical Engineering Journal* **2022**, *433*, 133832.

[30] S. Tao, I. Schmidt, G. Brocks, J. Jiang, I. Tranca, K. Meerholz, S. Olthof, *Nat Commun* **2019**, *10*, 2560.

[31] D.-K. Lee, N.-G. Park, *Appl Phys Rev* **2023**, *10*, 011308.

[32] K. Yeom, N. Park, *Solar RRL* **2024**, *8*, 2400068.

[33] D. B. Khadka, Y. Shirai, M. Yanagida, T. Tadano, K. Miyano, *Chemistry of Materials* **2023**, *35*, 4250.

[34] M. E. Kayesh, T. H. Chowdhury, K. Matsuishi, R. Kaneko, S. Kazaoui, J. J. Lee, T. Noda, A. Islam, *ACS Energy Lett* **2018**, *3*, 1584.

[35] Z. Lan, Y. Wang, J. Shao, D. Ma, Z. Liu, D. Li, Y. Hou, J. Yao, Y. Zhong, *Adv Funct Mater* **2024**, *34*, 2312426.

[36] B. Yu, Y. Sun, J. Zhang, K. Wang, H. Yu, *Small* **2024**, *20*, 2307025.

[37] D. B. Khadka, Y. Shirai, M. Yanagida, T. Masuda, K. Miyano, *Sustain Energy Fuels* **2017**, *1*, 755.

[38] A. Nakane, H. Tampo, M. Tamakoshi, S. Fujimoto, K. M. Kim, S. Kim, H. Shibata, S. Niki, H. Fujiwara, *J Appl Phys* **2016**, *120*, 064505.

[39] J. Zhu, S. Park, O. Y. Gong, C. Sohn, Z. Li, Z. Zhang, B. Jo, W. Kim, G. S. Han, D. H. Kim, T. K. Ahn, J. Lee, H. S. Jung, *Energy Environ Sci* **2021**, *14*, 4903.

[40] D. B. Khadka, Y. Shirai, M. Yanagida, H. Ota, A. Lyalin, T. Taketsugu, K. Miyano, *Nat Commun* **2024**, *15*, 882.

[41] C. Wang, F. Gu, Z. Zhao, H. Rao, Y. Qiu, Z. Cai, G. Zhan, X. Li, B. Sun, X. Yu, B. Zhao, Z. Liu, Z. Bian, C. Huang, *Adv Mater* **2020**, *32*, 1907623.

[42] C. Ding, Y. Zhang, F. Liu, Y. Kitabatake, S. Hayase, T. Toyoda, K. Yoshino, T. Minemoto, K. Katayama, Q. Shen, *Nano Energy* **2018**, *53*, 17.

[43] D. B. Khadka, Y. Shirai, M. Yanagida, K. Miyano, *ACS Appl Energy Mater* **2021**, *4*, 12819.

[44] S. Hu, K. Otsuka, R. Murdey, T. Nakamura, M. A. Truong, T. Yamada, T. Handa, K. Matsuda, K. Nakano, A. Sato, K. Marumoto, K. Tajima, Y. Kanemitsu, A. Wakamiya, *Energy Environ Sci* **2022**, *15*, 2096.

[45] E. Hou, J. Chen, J. Luo, Y. Fan, C. Sun, Y. Ding, P. Xu, H. Zhang, S. Cheng, X. Zhao, L. Xie, J. Yan, C. Tian, Z. Wei, *Angewandte Chemie* **2024**, *136*, e202402775.

[46] D. B. Khadka, Y. Shirai, M. Yanagida, K. Miyano, *ACS Appl Energy Mater* **2021**, *4*, 11121.

[47] K. Miyano, M. Yanagida, Y. Shirai, *Adv Energy Mater* **2020**, *10*, 1903097.

[48] K. Momma, F. Izumi, *J Appl Crystallogr* **2011**, *44*, 1272.

[49] G. Kresse, J. Furthmüller, *Phys Rev B* **1996**, *54*, 11169.

[50] G. Kresse, D. Joubert, *Phys Rev B* **1999**, *59*, 1758.

[51] J. P. Perdew, A. Ruzsinszky, G. I. Csonka, O. A. Vydrov, G. E. Scuseria, L. A. Constantin, X. Zhou, K. Burke, *Phys Rev Lett* **2008**, *100*, 136406.

Table of content graphics

The WB-Sn-perovskite solar cells with molecular surface treatment using 4-Fluoro-benzohydrazide achieved a device efficiency of 11.14%. This enhancement is attributed to the suppression of the Sn^{2+} oxidation, modulation of surface chemistry and interfacial energy band, and mitigation of the defect in the WB-Sn-HP film.